Eur. Phys. J. A **16**, 371–379 (2003)
DOI 10.1140/epja/i2001-10270-4

THE EUROPEAN PHYSICAL JOURNAL A

Implication of proton-nucleus scattering for density distributions of unstable nuclei

M. Rashdan[a]

Department of Mathematics and Theoretical Physics, Atomic Energy Authority, Cairo, Egypt

Received: 1 December 2001 / Revised version: 5 July 2002 /
Published online: 11 February 2003 –
Communicated by P. Schuck

Abstract. The use of elastic proton scattering at intermediate and high energies to obtain information about the density distributions of unstable nuclei is investigated. A comparison between the relativistic impulse approximation (RIA) and Glauber model for proton scattering from ^{16}O, ^{40}Ca, ^{44}Ca and ^{48}Ca at medium energies is performed. We used density distributions derived from the relativistic mean-field theory, employing the recent relativistic force NL-RA1, as well as experimental and phenomenological densities. It is found that the eikonal approximation can describe the cross-section only at small scattering angles and is weakly sensitive to the density distributions, while the RIA nicely produced the experimental cross-sections, even at medium and larger angles, and was very sensitive to the nuclear densities. Furthermore, the RIA better describes the isospin dependence of the cross-section. We used the RIA to investigate the density distribution of ^{58}Ca for proton scattering at different energies. It is found that the cross-section strongly depends on the parameters of the density distribution even at a small scattering angle. These results are important in extracting information about the structure of unstable nuclei. We also investigated the RIA and its sensitivity in describing halo nuclei such as ^{6}He. We used for ^{6}He a no-halo Gaussian density and a realistic-halo density that derived in the cluster orbital shell model approximation and contains the extended distribution of the valence nucleons. Comparison with the recent experimental data at GSI at 717 MeV/nucleon shows that the RIA successfully described the data at all considered range of the momentum transfer and on the other hand favor the halo structure of ^{6}He.

PACS. 24.10.Jv Relativistic models – 25.60.-t Reactions induced by unstable nuclei

1 Introduction

The study of unstable nuclei is one of the most interesting subjects in nuclear physics. Several kinds of data can be used to study the structure of nuclei far from stability such as reaction cross-sections and momentum distributions of fragments [1,2]. Elastic proton scattering could also be expected to provide detailed information about the structure of unstable nuclei such as neutron skins and halo structure, although recent investigations of Weppner *et al.* [3] indicated that elastic proton scattering at intermediate energy could not provide constraints on the features of the structure. Similar conclusion of Weppner *et al.* has also been drawn by Korsheninnikov *et al.* [4] from their detailed investigations of proton elastic scattering from halo nuclei, using an eikonal approach.

Current microscopic nonrelativistic scattering theories form the proton-nucleus optical potentials by calculation of the t or g matrices in a momentum or a coordinate space representation. The details of these nonrelativistic proton-nucleus scattering theories are well covered in the review of Amos *et al.* [5]. At intermediate and high energies many authors used the Glauber multiple scattering [6] or eikonal approximation in describing particle-nucleus or nucleus-nucleus scattering and reactions (see for example [7,8]). Although the eikonal approximation is useful for describing scattering at forward angles, its use for medium and large scattering angles needs to be examined.

On the other hand, there has been considerable interest in recent years in a relativistic description of proton-nucleus scattering [9–17]. In fact, relativistic approaches are a dramatic improvement of nonrelativistic ones. For example, the spin-orbit interaction is built in the relativistic Dirac equation that described the interacting nucleons without any need for adjustable parameters. Another important feature of the relativistic description of the nuclear many-body problem is quite the description of nuclear-matter saturation, where most of the microscopic nonrelativistic approaches saturate nuclear matter at densities larger than the normal nuclear-matter density. Thus, the

[a] e-mail: mrashdan@hotmail.com

relativistic description of the nuclear many-body problem satisfies a consistent description of both nuclear matter and nuclear scattering.

As concerning proton-nucleus scattering relativistic impulse approximation [9–17] (RIA) calculations have provided a remarkably good description of the elastic cross-section and spin observables at laboratory kinetic energy of 500 MeV and above. These calculations have been extended to lower energies by including modifications due to exchange and Pauli-blocking effects, rather than delta-resonance influences, which are more important above the pion threshold [16,17].

In the RIA the motion of the projectile in the field of the nucleus is described with the Dirac equation. The target structure can also be described in terms of Dirac nucleons, where the target nucleons interact with each other through static mean fields of Lorentz scalar and vector character; these fields are produced by the scalar and number densities of the nucleons, so that the ground state can be calculated self-consistently.

The aim of the present work is to investigate the RIA in extracting information about the structure of unstable nuclei. First, we perform a comparison between the RIA and the eikonal approximation, which is widely used in describing proton-nucleus scattering, as well as in investigating the sensitivity of these models to the density distributions. We used densities derived from the relativistic mean-field (RMF) theory [18–31], employing the recent relativistic force NL-RA1 [19], as well as experimental and phenomenological densities. We carried out our study on proton elastic scattering from ^{16}O, ^{40}Ca, ^{44}Ca, ^{48}Ca and ^{58}Ca. Furthermore, we investigated the sensitivity of the elastic proton scattering cross-section, calculated in the RIA, to the halo structure of halo nuclei such as ^{6}He. A realistic-halo density derived in the cluster orbital shell model calculations (COSM) [32,4] is used for describing the halo structure of ^{6}He. Section 2 presents the theoretical description. The results are presented and discussed in sect. 3. The effect of the halo structure in ^{6}He is discussed in sect. 4. Finally, sect. 5 presents a summary and conclusion.

2 Theoretical description

In the relativistic impulse approximation the Dirac equation for the single-particle motion of the projectile nucleon in the mean field of the target nucleus can be written as [9–17]

$$[-i\alpha\cdot\nabla+U_{\rm V}(r;E)+\beta(M+U_{\rm S}(r;E))+V_{\rm C}]|\psi\rangle=E|\psi\rangle, \tag{1}$$

where $U_{\rm S}$ and $U_{\rm V}$ are the scalar and vector potentials which contain both direct and exchange parts,

$$U_{\rm L(=S,V)}\equiv U_{\rm L}^{\rm D}(r;E)+U_{\rm L}^{\rm X}(r;E), \tag{2}$$

E is the total nucleon-nucleus CM projectile energy, M is its rest mass and $V_{\rm C}$ is the Coulomb potential energy. The Dirac optical potentials are calculated from the nucleon-nucleon (NN) t-matrix, where the action of these potentials on the incident-projectile wave function, projected in the coordinate space, can be written as [15–17],

$$\langle x|U_{\rm opt}|\psi_0\rangle=-\frac{4\pi ip}{M}\sum_{\alpha}^{\rm occ}\int {\rm d}^3y'\int {\rm d}^3y\int {\rm d}^3x'\,\overline{\psi_\alpha}\times\left[\langle xy'|t(E)|x'y\rangle+(-1)^{\rm T}\langle y'x|t(E)|x'y\rangle\right]\psi_0(x')\psi_\alpha(y)\,, \tag{3}$$

where

$$U_{\rm opt}=U_{\rm S}+\gamma^0U_{\rm V}, \tag{4}$$

p is the magnitude of the three-momentum of the projectile in the nucleon-nucleus CM frame and T is the total isospin of the two-nucleon state. The antisymmetrized matrix element of $t(E)$ in coordinate space is the Fourier transform of the momentum space matrix element. The t-matrix $t(E)$ is the lowest-order meson-exchange diagram evaluated from the Feynman rules. The mesons have different spins and parities (scalar, vector, tensor, pseudoscalar, and axial vector) and isospin 0 and 1. The Dirac optical potentials (direct and exchange parts) are written as a folding integral of the nucleon-nucleon t-matrix and the target (scalar and vector) densities [16,17],

$$U_{\rm L}^{\rm D}(r;E)=-\frac{4\pi ip}{M}\int {\rm d}^3r'\rho_{\rm L}(\mathbf{r}')\;t_{\rm L}^{\rm D}(|\mathbf{r}-\mathbf{r}'|;E),, \tag{5}$$

$$U_{\rm L}^{\rm X}(r;E)=-\frac{4\pi ip}{M}\int {\rm d}^3r'\rho_{\rm L}(\mathbf{r},\mathbf{r}')\;t_{\rm L}^{\rm X}(|\mathbf{r}-\mathbf{r}'|;E)\times j_0\left(\frac{p}{\hbar}|\mathbf{r}-\mathbf{r}'|\right), \tag{6}$$

where the local density approximation is used for the nonlocal exchange term and

$$t_{\rm L}^{\rm D,X}(s;E)=\int\frac{{\rm d}^3q}{2\pi^3}\;t_{\rm L}^{\rm D,X}(\mathbf{q};E)e^{-i\mathbf{q}\cdot\mathbf{s}}. \tag{7}$$

The off-diagonal density matrix $\rho_{\rm L}(\mathbf{r},\mathbf{r}')$ is approximated to be given in terms of the one-body densities, using the density matrix expansion approximation [16,17]. For the NN t-matrix we used the parameterization of [15,16]. For laboratory energies around 500 MeV, the Dirac optical potentials are modified by a Pauling-blocking correction [16,17]

$$U_{\rm L}(r;E)=\left[1-a(E)\left(\frac{\rho_{\rm B}(r)}{\rho_0}\right)^{2/3}\right]U_{\rm L}(r;E). \tag{8}$$

Here, $\rho_{\rm B}(r)$ is the local baryon density and ρ_0 is the normal nuclear-matter density. The Pauli-blocking factor $a(E)$ has been obtained by performing a Dirac-Brueckner calculation using a one-boson-exchange potential, where it can be used for energies near 200–500 MeV [16,17].

As for the scalar and vector (baryon) densities of the target nucleus we derived them from the Lagrangian density of the relativistic mean-field theory [18–31]. This Lagrangian describes Dirac nucleons interacting with the

scalar self-coupling σ-meson field Φ, the self-coupling neutral vector ω-meson field $\mathbf{V}^{\mu}(\mu = 0, 1, 2, 3)$, the isovector-vector ρ-meson field $\overrightarrow{\rho}^{\mu}$ and the electromagnetic fields A^{μ}, *i.e.*,

$$
\begin{aligned}
L = & \overline{\psi_i}\left(\gamma^{\mu} i\partial_{\mu} - M\right)\psi_i + \frac{1}{2}\partial^{\mu}\Phi\partial_{\mu}\Phi - \frac{1}{2}m_{\sigma}^{2}\Phi^{2} \\
& - \frac{1}{3}b_2\Phi^{3} - \frac{1}{4}b_3\Phi^{4} - g_{\sigma}\overline{\psi_i}\psi_i\Phi - \frac{1}{4}\Omega^{\mu\nu}\Omega_{\mu\nu} \\
& + \frac{1}{2}m_{\omega}^{2}\mathbf{V}^{\mu}\mathbf{V}_{\mu} - g_{\omega}\overline{\psi_i}\gamma^{\mu}\psi_i\mathbf{V}_{\mu} - \frac{1}{4}\overrightarrow{\mathbf{B}}^{\mu\nu}\overrightarrow{\mathbf{B}}_{\mu\nu} \\
& + \frac{1}{2}m_{\rho}^{2}\overrightarrow{\rho}^{\mu}\overrightarrow{\rho}_{\mu} - g_{\rho}\overline{\psi_i}\gamma^{\mu}\overrightarrow{\tau}\psi_i\overrightarrow{\rho}_{\mu} \\
& - \frac{1}{4}\mathbf{F}^{\mu\nu}\mathbf{F}_{\mu\nu} - e\overline{\psi_i}\gamma^{\mu}\frac{1+\tau_{3i}}{2}\psi_i\mathbf{A}_{\mu}. \qquad (9)
\end{aligned}
$$

Arrows denote vectors in isospin space. The Dirac spinor ψ_i represents the nucleon with mass M. m_{σ}, m_{ω}, and m_{ρ} are the masses of the σ-meson, the ω-meson, and the ρ-meson, respectively. The meson-nucleon coupling constants, g_{σ}, g_{ω} and g_{ρ}, and the meson masses are parameters adjusted to fit nuclear-matter data and some static properties of finite nuclei. $\Omega^{\mu\nu}$, $\overrightarrow{\mathbf{B}}^{\mu\nu}$ and $F^{\mu\nu}$ are field tensors. τ_3 is the third component of the isospin.

For the masses and coupling constants of the Lagrangian density (9) we used the recent parameter set NL-RA1 [19]: $M = 939\,\mathrm{MeV}$, $m_{\sigma} = 515.7\,\mathrm{MeV}$, $m_{\omega} = 783\,\mathrm{MeV}$, $m_{\rho} = 763\,\mathrm{MeV}$, $g_{\sigma} = 10.36231$, $g_{\omega} = 12.921154$, $g_{\rho} = 4.4058795$, $b_2 = -10.059947\,\mathrm{fm}^{-1}$ and $b_3 = -27.5565$. Figure 1 shows the densities of ^{16}O and ^{48}Ca calculated by solving the Euler-Lagrange field equations derived from the relativistic Lagrangian density (9) and using the parameter set NL-RA1 (see ref. [19] for more details).

We also used two parameters Fermi (2PF) ($\omega = 0$) and 3PF density distributions of the following modified Woods-Saxon (W-S) shape:

$$
\rho_p(r) = \frac{\rho_{0p}}{1 + e^{(r-R_0^p)/a_p}}\left(1 + \omega\left(\frac{r}{R_0^p}\right)^2\right). \qquad (10)
$$

The experimental parameters of the proton densities are listed in [33]. The neutron density distributions are taken as the proton ones, but with increasing the neutron radius by the neutron excess, *i.e.*,

$$
R_0^n = R_0^p + \alpha\frac{N-Z}{A}, \qquad (11)
$$

where α is a scaling parameter taken to be 1 fm. N, Z and A are the neutron, proton and mass numbers of the target nucleus. The neutron diffuseness a_n is, in general, taken equal to the proton one. The scalar densities are assumed equal to the vector densities, *i.e.*, $\rho_{\mathrm{s}}^{p} = \rho_p$ and $\rho_{\mathrm{s}}^{n} = \rho_n$. This approximation is only used when experimental or nonrelativistic densities are used in the calculations, while for the RMF case all the proton and neutron scalar and vector densities are derived from the relativistic Lagrangian (9).

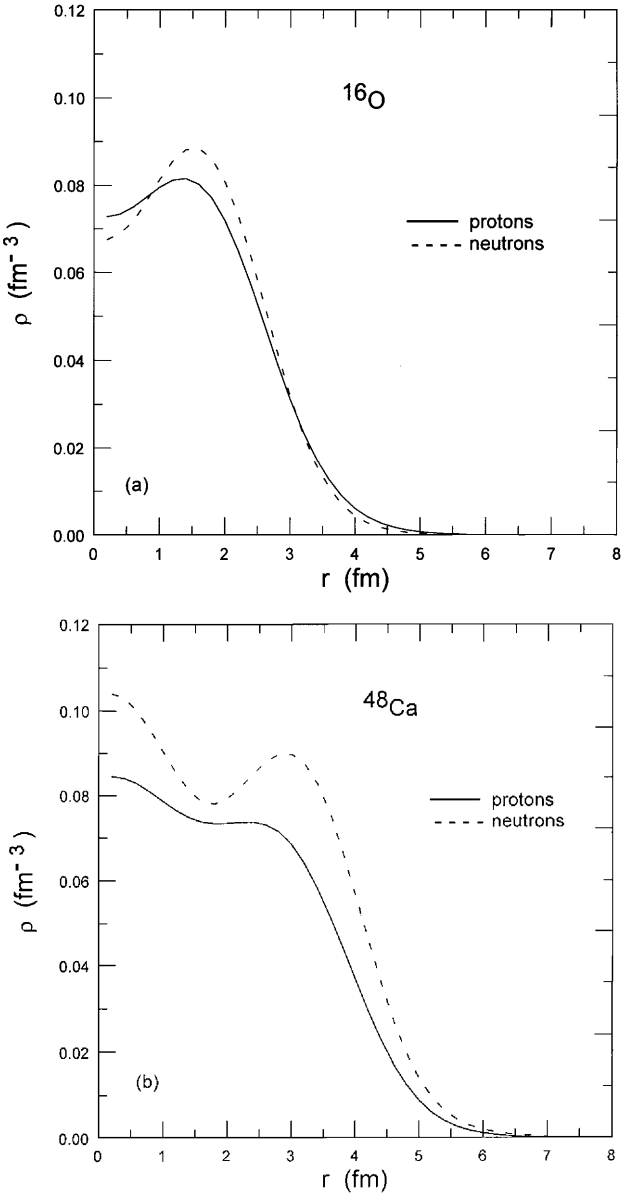

Fig. 1. (a) The proton and neutron densities of ^{16}O calculated by solving the field equations derived from the relativistic mean-field Lagrangian density (9) using the parameter set NL-RA1. (b) Same as (a) but for ^{48}Ca.

3 Results

The elastic scattering of $p + {}^{16}\mathrm{O}$ at $E_{\mathrm{lab}} = 317.4$ MeV, which is calculated in the relativistic impulse approximation, as well as in the eikonal approximation, using densities derived from the RMF theory, and employed the relativistic force NL-RA1, is shown in fig. 2(a). The eikonal approximation which is used in this work is fully described in ref. [7]. Figure 2(b) shows the analyzing power calculated in RIA in comparison with experiment. Figure 3 is the same as fig. 2(a) but at $E_{\mathrm{lab}} = 497.5$ MeV. The experimental data at these two values of energy are taken from refs. [34] and [35], respectively. As shown from these figures, the RIA better described the data even at large

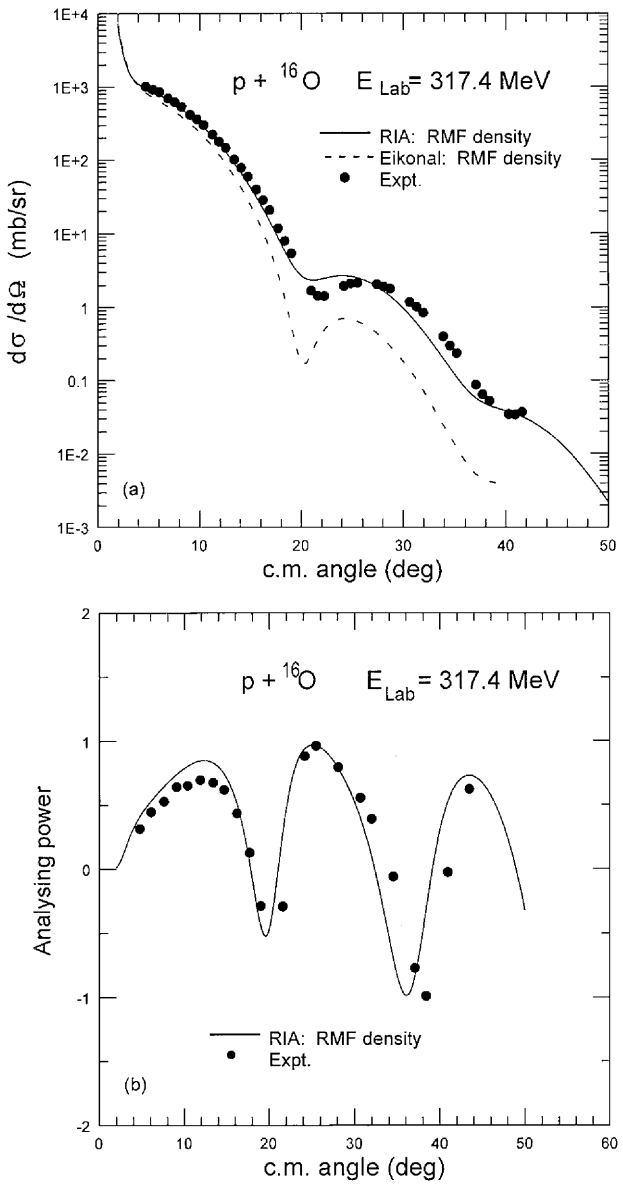

Fig. 2. (a) The elastic-scattering cross-section of $p + {}^{16}\mathrm{O}$ calculated in the relativistic impulse approximation and eikonal approximation at $E_{\mathrm{lab}} \approx 318$ MeV/nucleon using densities derived from the RMF Lagrangian (12), employing the relativistic force NL-RA1, in comparison with the experimental data [34]. (b) Same as (a) but for the analyzing power, calculated in the RIA.

scattering angles. This is also shown in figs. 4-7 for proton scattering from Ca isotopes (the experimental data are taken from refs. [36–38]). The eikonal approximation can describe the data only at small scattering angles, as shown from the figures, and its sensitivity to the nuclear densities has been found to be weak. Figures 4-7 show also that the relativistic impulse approximation better described the isospin dependence of the target nuclei. This is important for extracting information about unstable nuclei.

It is worth mentioning that in the eikonal calculations of the cross-section we neglect the spin-orbit potential

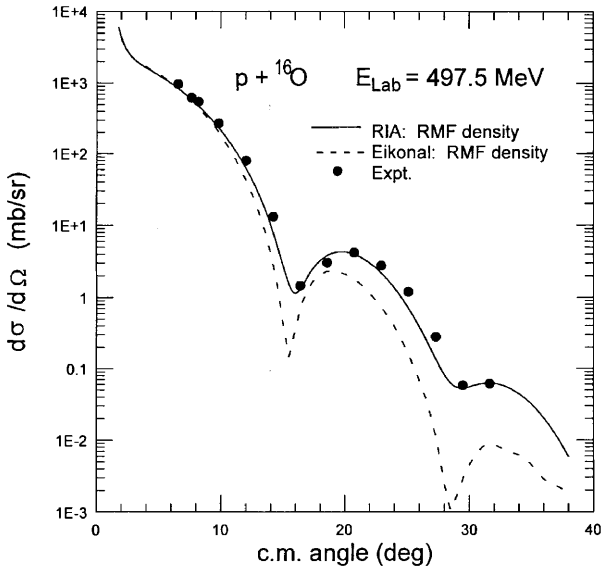

Fig. 3. Same as fig. 2(a) but at $E_{\mathrm{lab}} \approx 500$ MeV/nucleon. The experimental data are taken from [35].

since the parameters of this term are taken phenomenologically in all nonrelativistic calculations such as the eikonal model. Therefore, including this term phenomenologically will add some ambiguities in extracting information about the nuclear structure. On the other hand, in the relativistic impulse approximation the spin-orbit potential is built in the Dirac equation without any adjustable free parameters. This makes the RIA more powerful and advantageous in extracting information about the structure of unstable nuclei.

In order to investigate the sensitivity of the RIA to the nuclear densities in some detail we plotted in fig. 7 the elastic scattering cross-section of $p + {}^{48}\mathrm{Ca}$ calculated in the RIA using Woods-Saxon density (2PF) with $R_0^p = 3.7369$ fm and $a_{\mathrm{p}} = 0.5245$ fm [33]. R_0^n is given by relation (11) and three values for the neutron diffuseness parameter, namely; $a_n = a_p = 0.5245$ fm (solid line), $a_n = 0.7$ fm (dashed line), and $a_n = 0.3$ fm (dash-dotted line) are considered. The scalar densities are taken equal to the matter densities. As shown from fig. 7 the experimental density predicts very well the fitting to the cross-section even at large scattering angles since it better describes the tail. Any small change (under the normalization condition) in the neutron diffuseness parameter strongly affects the cross-section , especially at medium and large scattering angles, where the cross-section decreases by increasing the diffuseness and vice versa. This is due to the Dirac optical potentials, which were strongly reduced in the inner region and extended to larger distances by increasing the diffuseness. This reduction in the Dirac optical potentials reduces the elastic-scattering cross-section.

We applied the RIA in investigating and extracting information about the structure of nuclei with large value of isospin such as ${}^{58}\mathrm{Ca}$. Figure 8 shows the elastic-scattering cross-section of $p + {}^{58}\mathrm{Ca}$ calculated in the RIA at 200, 300, and 400 MeV/nucleon, respectively, using 2PF as in fig. 7,

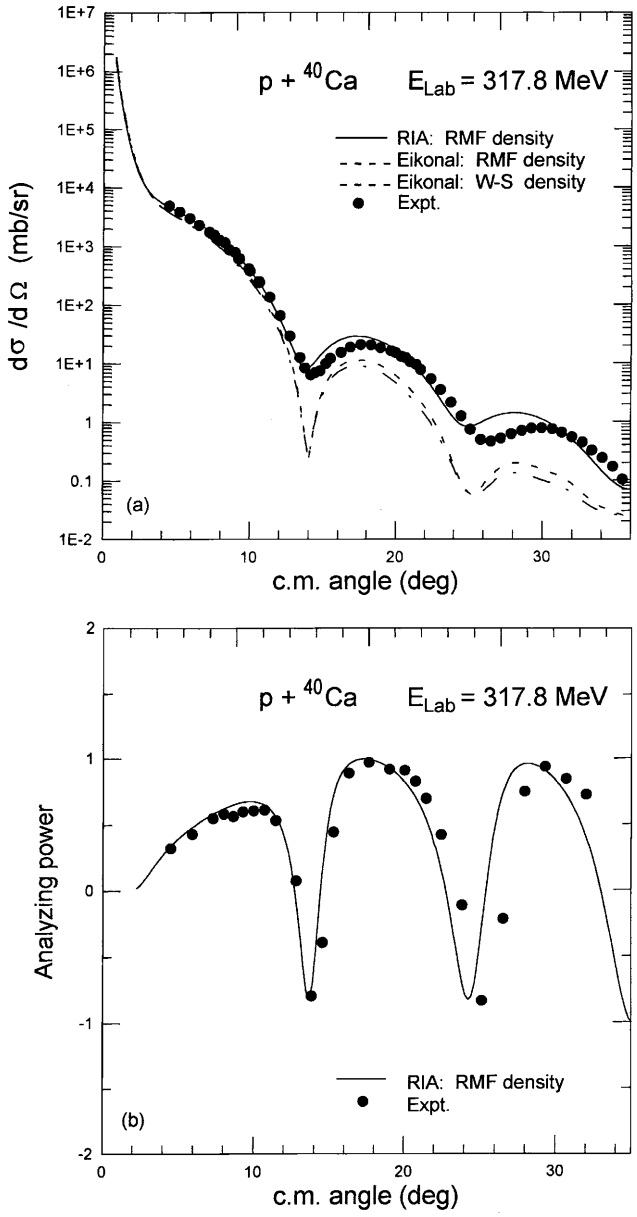

Fig. 4. (a) Same as fig. 2(a) but for $p + {}^{40}$Ca. (b) Same as fig. 2(b) but for $p + {}^{40}$Ca. The experimental data are taken from [36].

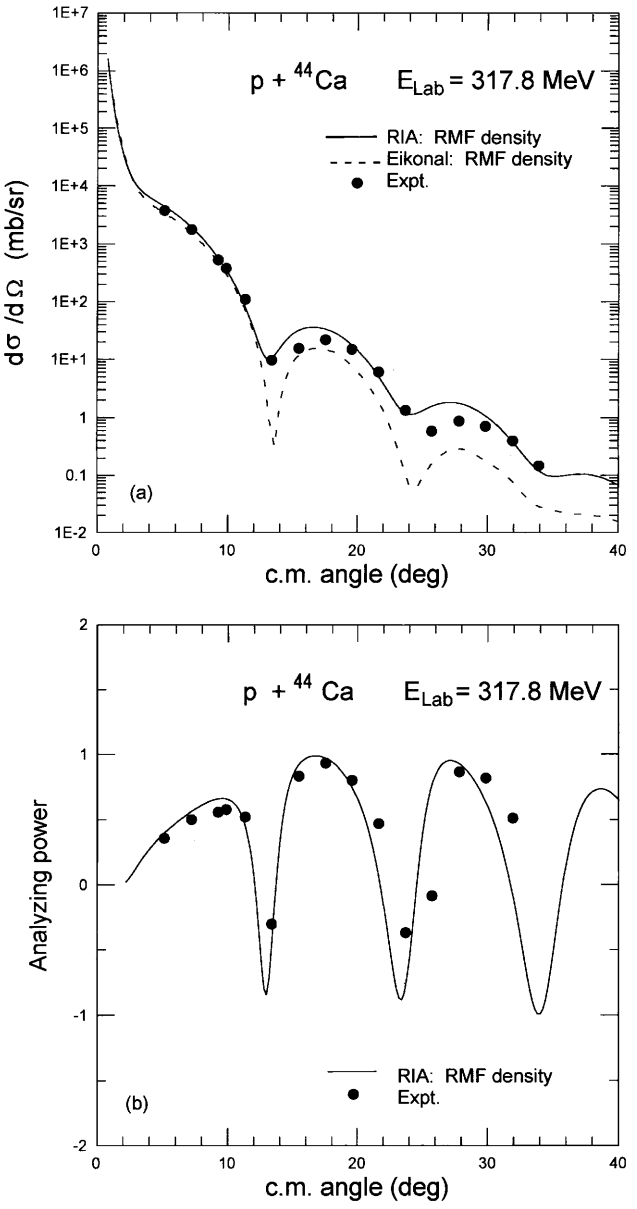

Fig. 5. (a) Same as fig. 4(a) but for the elastic scattering of $p + {}^{44}$Ca. (b) Same as fig. 4(b) but for the analyzing power. The experimental data are taken from [37].

for the three values of the neutron diffuseness parameter $a_n = 0.6$, 1, and 1.4 fm. As shown from these figures the cross-section is strongly sensitive to the parameters of the nuclear density, where, in general, it decreases by increasing the neutron diffuseness parameter, even at small scattering angle, less than and around 10 degrees. The dip in the cross-section decreases and goes to the forward direction by increasing the energy. One also notices that the differences in the cross-section at very small angles (about 5 degrees) due to the changes in the diffuseness parameter increase by increasing the energy. We expect these results to be important for experiments in extracting information about exotic and halo nuclei.

4 The effect of halo structure

In this section, we investigate RIA in describing proton scattering from halo nuclei. We consider, as an example, the angular distribution of proton scattering from the two-neutron halo nucleus ^{6}He. In order to study the effect of the two-neutron halo, we assumed a Gaussian model for the proton and neutron density distributions of the target nucleus with equal proton and neutron oscillator parameter: 1.55 fm. We call this model the no-halo model. The corresponding proton and neutron densities are shown in fig. 9(a). As can be seen from this figure there is no halo in the neutron density distribution. To describe the halo structure of ^{6}He we used the halo density derived in the

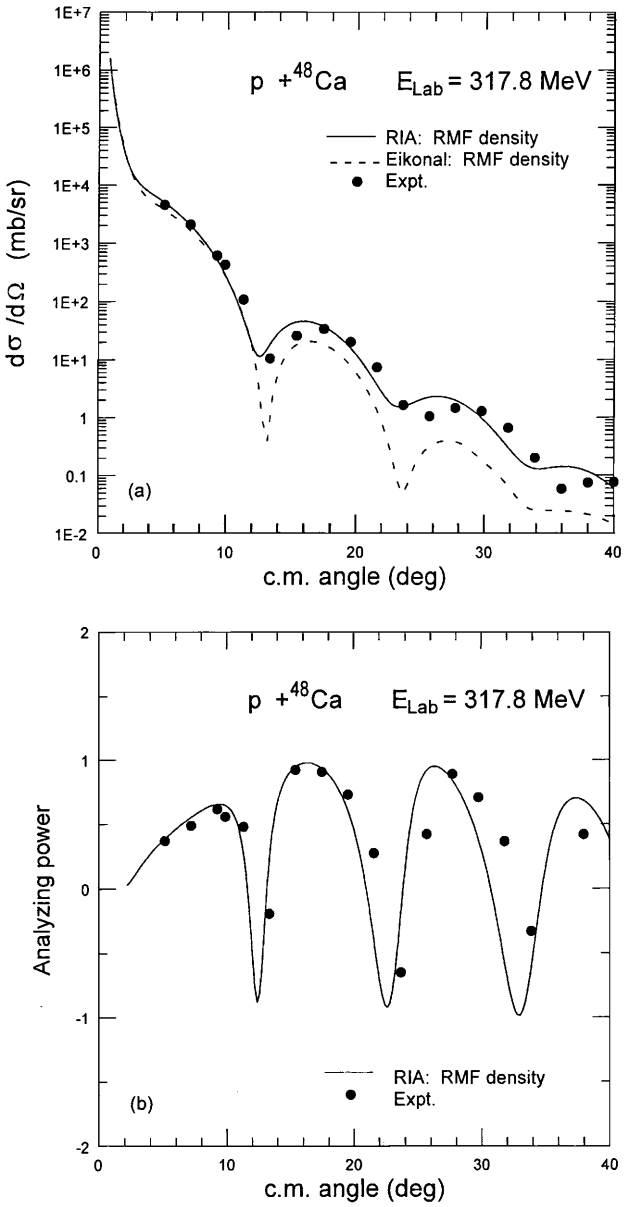

Fig. 6. (a) Same as fig. 4(a) but for the elastic scattering of $p + {}^{48}$Ca. (b) Same as fig. 4(b) but for the analyzing power. The experimental data are taken from [38].

cluster orbital shell model approximation [32,4]. This density contains the extended distribution of the valence nucleons and corresponds to the experimental matter radius of ^{6}He and it can be written as

$$\rho_{i(=p,n)}(r) = N_{ci}\frac{\exp(-r^2/a^2)}{\pi^{3/2}a^3} + N_{vi}\frac{2\exp(-r^2/b^2)}{3\pi^{3/2}b^5} \times \left[Ar^2 + B\left(r^2 - \frac{3}{2}b^2\right)^2\right]. \quad (12)$$

For ^{6}He (α+2n model); $N_{cp} = N_{cn} = 2, N_{vp} = 0, N_{vn} = 2$, $A = 1$, $B = 0$. The parameter $a = 1.55$ fm corresponding to a Gaussian density for ^{4}He folded with a Gaussian for the α-core motion, which characterizes the radius of ^{6}He.

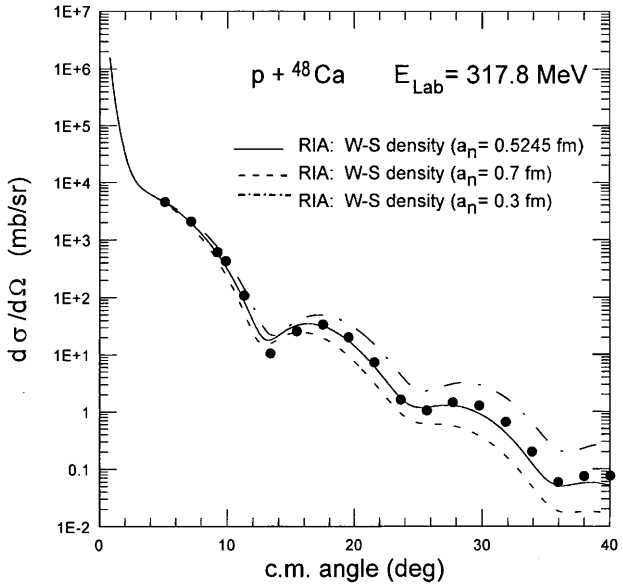

Fig. 7. The elastic scattering of $p+{}^{48}$Ca calculated in the RIA using Woods-Saxon shape (2PF) and using three values of the neutron diffuseness parameter, $a_n = 0.5245$ fm (solid line), 0.7 fm (dashed line), and 0.3 fm (dash-dotted line).

The parameter b is taken as $b = 2.24$ fm [4]. This density is plotted in fig. 9(b). Increasing the parameter b the neutron halo increases as shown from fig. 9(c). Then we calculated the cross-section of $p + {}^6$He using these model densities. The scalar densities are taken as the vector ones, *i.e.*, $\rho_{\rm s}^p = \rho_p$ and $\rho_{\rm s}^n = \rho_n$.

Figure 10 shows the elastic scattering cross-section of $p+{}^6$He calculated in the RIA at 300 MeV using densities without (solid line) and with (dashed line) halo strucutre, *i.e.* using the densities plotted in fig. 9 ((a) and (b)). As shown from fig. 10 the effect of the two-neutron halo structure in ^{6}He strongly affects the cross-section, especially at medium and large scattering angles. This is due to the Dirac optical potentials, where weaker potentials were obtained in the inner regions when halo densities are used, as shown from fig. 11. One also notices that by increasing the scattering angle the difference between the cross-sections calculated with and without including the halo structure in the nuclear densities increases.

As an application of these calculations, we investigated the recent data at GSI for $p+{}^6$He elastic scattering at 717 MeV/nucleon [39]. Figure 12 shows the differential cross-section for proton elastic scattering from ^{6}He against the invariant four-momentum transfer at 717 MeV/nucleon calculated in the RIA in comparison with the experimental data [39]. The solid line represents the calculation using the no-halo Gaussian density, plotted in fig. 9(a), while the dashed line represents the calculation using the realistic cluster orbital shell model halo density plotted in fig. 9(b). The dotted line represents the calculation using the COSM halo density plotted in fig. 9(c). As shown from this figure the COSM halo density, in general, successfully describes the cross-section, while the no-halo Gaussian density presents a cross-section much higher than

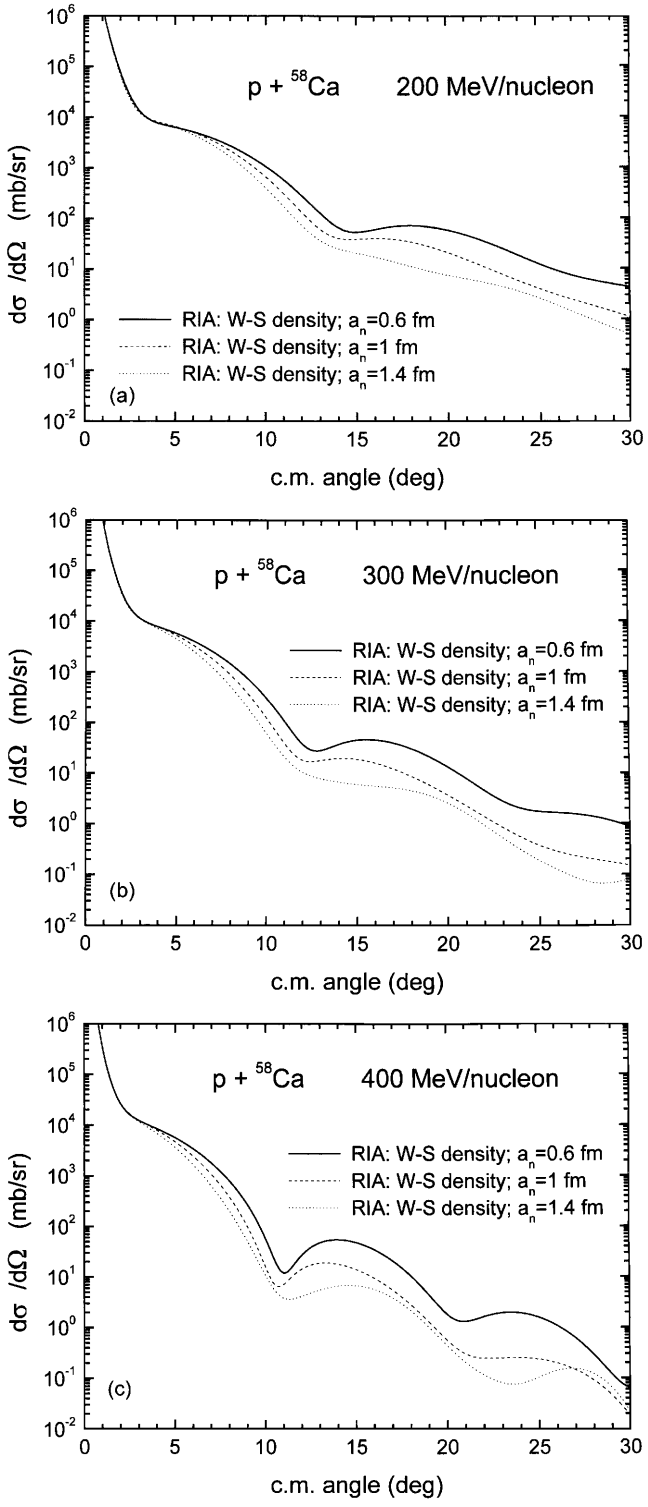

Fig. 8. (a) Same as fig. 7 but for the elastic scattering of $p+^{58}$Ca at 200 MeV/nucleon and using the values $a_n = 0.6$ fm (solid line), 1 fm (dashed line) and 1.4 fm (dotted line) for the neutron diffuseness parameter. (b) Same as (a) but at 300 MeV/nucleon. (c) Same as (a) but at 400 MeV/nucleon.

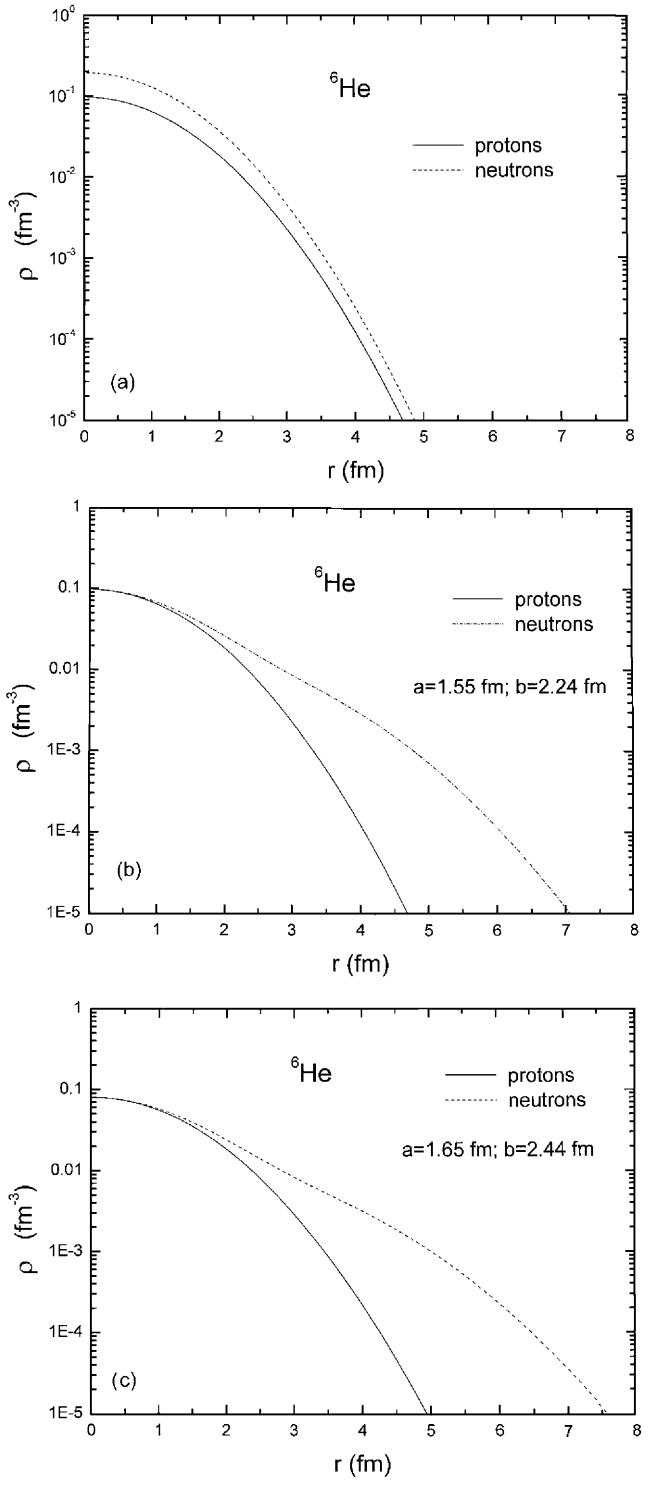

Fig. 9. (a) The no-halo Gaussian density distrinution of ^{6}He with equal proton and neutron oscillator parameter: 1.55 fm. (b) The cluster orbit shell model halo density (eq. (9)) with the parameters $a = 1.55$ fm and $b = 2.24$ fm. (c) Same as fig. 8(b) but for $a = 1.65$ fm and $b = 2.44$ fm.

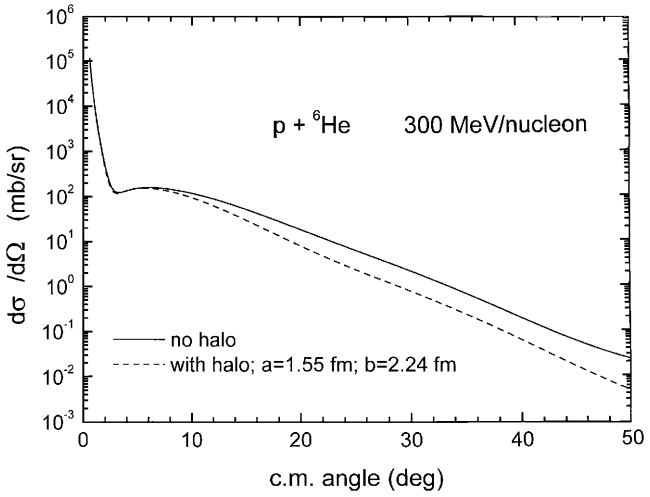

Fig. 10. The elastic-scattering cross-section of $p + {}^6\mathrm{He}$ calculated at $E_{\mathrm{Lab}} = 300$ MeV/nucleon in the RIA and using the no-halo Gaussian density and the COSM halo density distributions, which are plotted in fig. 9 (a,b).

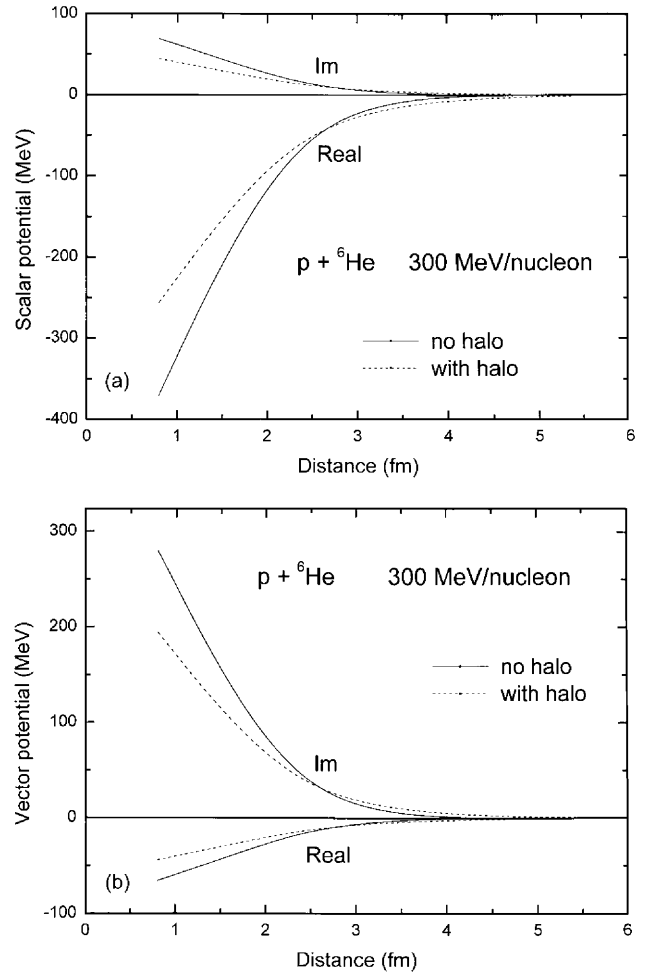

Fig. 11. (a) The Dirac scalar optical potentials calculated for $p + {}^6\mathrm{He}$ at $E_{\mathrm{Lab}} = 300\,\mathrm{MeV}$ using the no-halo Gaussian and halo COSM densities plotted in fig. 9 (a,b). The scalar densities are taken to equal the vector densities. (b) Same as (a) but for the Dirac vector optical potentials.

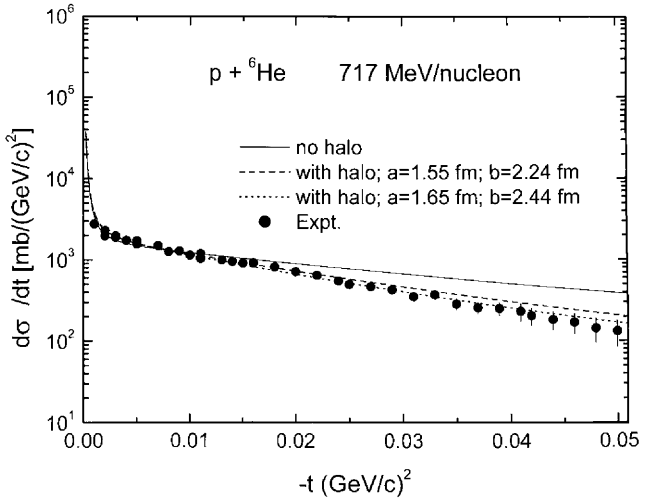

Fig. 12. The elastic-scattering cross-section of $p + {}^6\mathrm{He}$ calculated at 717 MeV/nucleon against the invariant four-momentum transfer in the RIA using the no-halo Gaussian density (solid line) and the halo COSM density (dashed line) distributions plotted in fig. 9 (a,b). The dotted line corresponds to the cross-section calculated by the COSM halo density which is plotted in fig. 9(c), where the parameters a and b are slightly increased to $a = 1.65$ fm and $b = 2.44$ fm.

the experimental data, especially at medium and large momentum transfer in disagreement with the data. One also notices that the small difference appearing at large momentum transfer between the data and the calculated cross-section using the COSM halo density with parameters $a = 1.55$ fm and $b = 2.24$ fm can be removed by a slight increase of these parameters to $a = 1.65$ fm and $b = 2.24$ fm (see fig. 9(c)), *i.e.* by increasing the halo effect, which, on the other hand, strongly refers to the halo structure of ^{6}He.

It is worth mentioning that in the analysis of the data of the GSI group using the eikonal approximation the slope parameter of the nucleon-nucleon amplitude is readjusted in order to fit the experimental cross-section [39]. Another disadvantage of the eikinal approximation is that the sensitivity of the calculated p-nucleus cross-section to the difference between the proton and neutron density distributions is expected to be weak, as it has been found in the previous section, since the difference between the elementary pp and pn cross-sections is relatively small.

5 Summary and conclusion

We have studied the validity of both the relativistic impulse approximation and eikonal approximation in describing elastic proton-nucleus scattering at intermediate energies. We used densities derived from the relativistic mean-field theory, employing the recent relativistic interaction NLRA1, as well as phenomenological and experimental densities. We found that the eikonal approximation can describe the cross-section at forward scattering angles and, more important, is weakly sensitive to the difference in the proton and neutron density distributions. On the

other hand, the RIA is found to better describe the observables even at medium and large scattering angles and it was very sensitive to the nuclear densities even at small scattering angles. This is due to the strong dependence of the vector and scalar Dirac optical potentials on nuclear densities. Furthermore, it has been found that the RIA better described the isospin dependence of the target nucleus in proton-nucleus scattering, which on the other hand is very important for extracting information about the structure of exotic and halo nuclei.

We applied the RIA for the recent data at GSI on $p + {}^6$He elastic scattering at 717 MeV/nucleon. A realistic cluster orbit shell model halo density is used in these investigations in addition to a Guassian no-halo density with an equal oscillator parameter for protons and neutrons. We found that the realistic COSM halo density better described the experimental data which favor the halo structure of ^{6}He.

References

1. I.Tanihata, Nucl. Phys. A **520**, 411c (1990); **522**, 275c; J. Phys. G **22**, 157 (1996).
2. P.G. Hansen, Nucl. Phys. A **533**, 89c (1993); P.G. Hansen, A.S. Jensen, B. Jonson, Annu. Rev. Nucl. Part. Sci. A **45**, 591 (1995).
3. S.P. Weppner, Ofir Garcia, Ch. Elster, nucl-th/0001029.
4. A.A. Korsheninnikov *et al.*, Nucl. Phys. A **616**, 189 (1997); **617**, 45(1997).
5. K. Amos *et al.*, Adv. Nucl. Phys. (2000).
6. R.J. Glauber, *High-Energy Collision Theory, Lectures in Theoretical Physics* (Interscience, New York, 1959) p. 315.
7. C.A. Bertulani, H. Sagawa, Nucl. Phys. A **588**, 667 (1995); C.A. Bertulani *et al.*, Phys. Rep. **226**, 281 (1993).
8. J.S. Al-Khalili, J.A. Tostevin, I.J. Thompson, Phys. Rev. C **54**, 1843 (1996).
9. J.A. McNeil, J.R. Shepard, S.J. Wallace, Phys. Rev. Lett. **50**, 1439 (1983).
10. J.R. Shepard, J.A. McNeil, S.J. Wallace, Phys. Rev. Lett. **50**, 1443 (1983).
11. B.C. Clark, S. Hama, R.L. Mercer, L. Ray, B.D. Serot, Phys. Rev. Lett. **50**, 1644 (1983).
12. B.C. Clark, S. Hama, R.L. Mercer, L. Ray, G.W. Hoffmann, B.D. Serot, Phys. Rev. C **28**, 1421 (1983).
13. B.C. Clark, S. Hama, R.L. Mercer, in *The Interaction Between Medium Energy Nucleons in Nuclei*, edited by H.O. Meyer, AIP Conf. Proc. Vol. **97** (AIP, New York, 1983) p. 260.
14. J.A. Tjon, S.J. Wallace, Phys. Rev. C **32**, 1667 (1985).
15. C.J. Horowitz, Phys. Rev. C **31**, 1340 (1985).
16. D.P. Murdock, C.J. Horowitz, Phys. Rev. C **35**, 1442 (1987).
17. L. Ray, G.W. Hoffmann, W.R. Coker, Phys. Rep. **212**, 223 (1992).
18. P.G. Reinhard, Rep. Prog. Phys. **52**, 439 (1989).
19. M. Rashdan, Phys. Rev. C **63**, (2001) 044303.
20. M. Rufa, P.G. Reinhard, J.A. Maruhn, W. Greiner, M.R. Strayer, Phys. Rev. C **38**, 390 (1988).
21. M. Rashdan, Phys. Rev. C **48**, 1848 (1993); Nucl. Phys. A **602**, 502 (1996); Phys. Rev. C **54**, 315 (1996); Int. J. Mod. Phys. E **6**, 151 (1997); M. Rashdan, Phys. Lett. B **395**, 141 (1997).
22. M.M. Sharma, M.A. Nagarajan, P. Ring, Phys. Lett. B **312**, 377 (1993).
23. P.G. Reinhard, M. Rufa, J. Maruhn, W. Greiner, J. Friedrich, Z. Phys. A **323**, 13 (1986).
24. Y. Sugahara, H. Toki, Nucl. Phys. A **579**, 557 (1994).
25. J.N. Ginocchio, Phys. Rev. Lett. **78**, 436 (1997).
26. T. Gonzalez-Llarena, J.L. Egido, G.A. Lalazissis, P. Ring, Phys. Lett. B **379**, 13 (1996).
27. W. Poeschl, D. Vretenar, G.A. Lalazissis, P. Ring, nucl-th/9709027.
28. G.A. Lalazissis, D. Vretenar, W. Poeschl, P. Ring, Nucl. Phys. A **632**, 363 (1998).
29. M. Stoitsov, P. Ring, D. Vretenar, G.A. Lalazissis, Phys. Rev. C **58**, 2086 (1998).
30. D. Vretenar, G.A. Lalazissis, P. Ring, Phys. Rev. Lett. **82**, 4595 (1999).
31. G.A. Lalazissis, D. Vretenar, P. Ring, M. Stoitsov, L. Robledo, Phys. Rev. C **60**, 014310 (1999).
32. M.V. Zhukov *et al.*, Phys. Rep. **231**, 151 (1993).
33. C.W. De Jager *et al.*, At. Data Nucl. Data Tables, **14**, 479 (74);.
34. J.J. Kelly *et al.*, Phys. Rev. C **44**, 1272 (1991).
35. B.S. Flanders *et al.*, Phys. Rev. C **43**, 2103 (1991).
36. J.J. Kelly *et al.*, Phys. Rev. C **44**, 2602 (1991); A.E. Feldman, PhD Thesis, University of Maryland, 1991.
37. P.H. Karen, PhD Thesis, University of Virginia, 1993.
38. A.E. Feldman *et al.*, Phys. Rev. C **49** 2068 (1993); A.E. Feldman, PhD Thesis, University of Maryland, 1991.
39. G.D. Alkhazov *et al.*, Phys. Rev. Lett. **78**, 2313 (1997).